

QUANTUM SIMULATION

Second Chern number of a quantum-simulated non-Abelian Yang monopole

Seiji Sugawa*[†], Francisco Salces-Carcoba, Abigail R. Perry[‡], Yuchen Yue, I. B. Spielman[†]

Topological order is often quantified in terms of Chern numbers, each of which classifies a topological singularity. Here, inspired by concepts from high-energy physics, we use quantum simulation based on the spin degrees of freedom of atomic Bose-Einstein condensates to characterize a singularity present in five-dimensional non-Abelian gauge theories—a Yang monopole. We quantify the monopole in terms of Chern numbers measured on enclosing manifolds: Whereas the well-known first Chern number vanishes, the second Chern number does not. By displacing the manifold, we induce and observe a topological transition, where the topology of the manifold changes to a trivial state.

The Yang-Mills theory is a non-Abelian gauge field theory that includes a higher gauge symmetry than quantum electrodynamics and now forms a cornerstone of the standard model of particle physics (1, 2). In the Yang-Mills theory, soliton solutions that include monopoles and instantons play a key role, theoretically describing phenomena in high-energy physics (3). The monopole solutions are sources of non-Abelian gauge fields and give rise to a nontrivial topology.

The physical importance of magnetic monopoles was captured in the seminal work by P. A. M. Dirac (4). Dirac considered a phase, now known as the Aharonov-Bohm phase, acquired by an electron with charge q_e moving around a magnetic monopole and showed that the monopole charge must be $q_m = nh/q_e$, where n is an integer and h is Planck's constant. Following from this quantization condition, Gauss's law for the magnetic field \mathbf{B} must take a quantized value $nh/q_e = \int_{S_2} \mathbf{B} \cdot d\mathbf{S}$, which essentially counts the number of magnetic charges inside the manifold S_2 [here S_2 is a closed two-dimensional (2D) surface and $d\mathbf{S} = \mathbf{n} dS$ (\mathbf{n} is a unit vector normal to the surface)]. The integral is topologically robust against deformation of the enclosing manifold as long as the number of monopoles enclosed is unchanged. The field from Dirac monopoles has been observed in a range of physical systems, and the associated topological charge—the first Chern number, often referred to as “the Chern number”—has been measured (5–7). The first Chern number and Abelian monopole field were measured in the parameter space of a spin-1/2 artificial atom (6, 7), and the Dirac monopole

analog was synthesized inside a spinor condensate where the associated spin texture was observed (5). In quantum mechanical systems, gauge fields such as the electromagnetic vector potential \mathcal{A} take central stage (in classical electromagnetism $\mathbf{B} = \nabla \times \mathcal{A}$) and are required to understand nature at the most fundamental level (8). The Yang-Mills theory is a non-Abelian extension of Dirac's magnetic monopole (9) and requires higher-order Chern numbers (higher-order than the first) for its topological characterization.

Here we report on the quantum simulation of a Yang monopole in a 5D parameter space built from an atomic quantum gases' internal states and the measurement of its topological charges by characterizing the associated non-Abelian gauge fields (often called curvatures). To extract the second and higher Chern numbers that result from non-Abelian gauge fields, we developed a method to evaluate the local non-Abelian

Berry curvatures through nonadiabatic responses of the system.

Monopole fields and Chern numbers

An \mathcal{N} dimensional vector gauge field $\mathcal{A}(\mathbf{q}) = (A_1, A_2, \dots, A_{\mathcal{N}})$, where $\mathbf{q} = (q_1, q_2, \dots, q_{\mathcal{N}})$ is the position, is said to be non-Abelian when the vector components $A_\mu(\mathbf{q})$ fail to commute, i.e., $[A_\mu, A_\nu] \neq 0$ ($\mu, \nu \in \{1, \dots, \mathcal{N}\}$), where μ and ν label the different vector components. The resulting curvature is given by

$$F_{\mu\nu}(\mathbf{q}) = \frac{\partial A_\nu}{\partial q_\mu} - \frac{\partial A_\mu}{\partial q_\nu} - i[A_\mu, A_\nu] \quad (1)$$

where i is an imaginary unit; in three spatial dimensions, the components of the magnetic field $B_\mu = \epsilon_{\mu\nu\lambda} F_{\nu\lambda}/2$, where λ is an integer, can be determined from the elements of the $F_{\nu\lambda}$ matrices ($\epsilon_{\mu\nu\lambda}$ is the rank-3 Levi-Civita symbol, and we used Einstein's implied summation convention for repeated indices). In analogy to the Gauss's law with electric charges (monopoles), the first Chern number is equivalently the integral

$$C_1 = \frac{1}{2\pi} \int_{S_2} \mathbf{B} \cdot d\mathbf{S} = \frac{1}{4\pi} \int_{S_2} F_{\mu\nu} dq_\mu \wedge dq_\nu \quad (2)$$

of the magnetic field \mathbf{B} or the Abelian field strength $F_{\nu\lambda}$ over a closed 2D manifold S_2 , where \wedge is the wedge product. The general n th Chern number of a non-Abelian gauge field is the n -wedge product of the non-Abelian curvature

$$\alpha_n C_n = \int_{S_{2n}} \text{tr}[F \wedge F \wedge F \wedge \dots \wedge F] d^{2n}S \quad (3)$$

where α_n ($\alpha_1 = 4\pi$, $\alpha_2 = 32\pi^2$, ...) is a normalization factor and S_{2n} is a closed $2n$ -dimensional manifold (10).

Chern numbers provide a topological classification of monopoles in gauge field theories. The monopoles are generally associated with

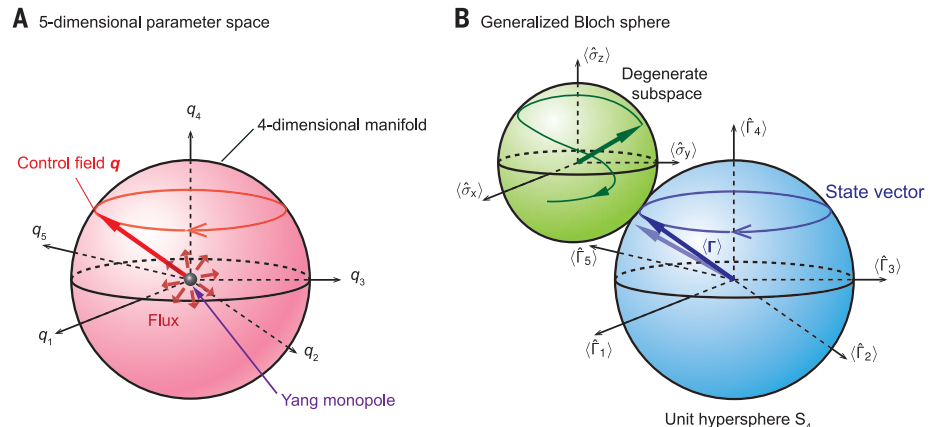


Fig. 1. Non-Abelian monopole and the appearance of nontrivial topology. (A) The 5D parameter space. The system has a topological defect at the origin, a Yang monopole, providing a source of non-Abelian gauge field. The topological invariant associated with the monopole is the second Chern number, defined on an enclosing 4D manifold. (B) Quantum states can be mapped onto generalized Bloch spheres. An additional Bloch sphere, which defines the wave function within each DS, is required to fully define our systems eigenstates. The 5D generalized magnetization vector Γ remains parallel with \mathbf{q} at adiabaticity, and the leading order correction to the adiabatic changes to \mathbf{q} , is a small deflection in Γ .

Joint Quantum Institute, National Institute of Standards and Technology and the University of Maryland, Gaithersburg, MD 20899-8424, USA.

*Present address: PRESTO, Japan Science and Technology Agency (JST), Saitama 332-0012, Japan, and Graduate School of Science, Kyoto University, Kyoto 606-8502, Japan.

†Corresponding author. Email: sugawa@yagura.scphys.kyoto-u.ac.jp (S.S.); ian.spielman@nist.gov (I.B.S.) ‡Present address: Georgia Tech Research Institute, Atlanta, GA 30318, USA.

a divergence in the field strength and can contribute a unit of flux through any enclosing manifold. This generalized flux is quantized and is given by the Chern numbers. In particular, for Yang monopoles, the first Chern number is zero, but the second Chern number is either +1 or -1 (Fig. 1).

Many quantum systems can be described by a Hamiltonian $\hat{H}(\mathbf{q})$ that depends on position \mathbf{q} in parameter space. At each position, the system is characterized by energies $E_\kappa(\mathbf{q})$ and eigenstates $|\kappa(\mathbf{q})\rangle$, where $\kappa \in \{1, \dots, \mathcal{K}\}$ is an index that identifies the eigenstate in our \mathcal{K} -dimensional Hilbert space. A gauge potential called the non-Abelian Berry connection $A_\mu^{\text{By}}(\mathbf{q}) = i\langle \beta(\mathbf{q}) | \partial / \partial q_\mu | \gamma(\mathbf{q}) \rangle$, where $\beta, \gamma \in \{1, \dots, \mathcal{K}\}$, is encoded in the wave functions; thus, for any position \mathbf{q} , each vector component A_μ is represented by a matrix. Chern numbers and curvatures can be then defined by Eqs. 1 to 3 for each well-separated energy level.

Because of these gauge fields, an initial quantum state can acquire a geometric phase as the location in parameter space is adiabatically changed. For nondegenerate quantum systems, the resulting geometric phase is called the Berry phase (11). A quantum state evolving within a degenerate subspace can acquire a Wilczek-Zee geometric phase, a matrix-valued generalization of the Berry phase obtained as the path-ordered line integral of a non-Abelian gauge potential (12–14).

Experimental Hamiltonian

We realized a non-Abelian gauge field by cyclically coupling four levels within the hyperfine ground states of rubidium-87 using radio-frequency and microwave fields (Fig. 2, A and B), essentially forming a square plaquette. The four couplings were parameterized by two Rabi frequencies Ω_A and Ω_B and two phases ϕ_A and ϕ_B arranged so that the sum of the phases around the plaquette was π . This configuration of control fields, along with a detuning $\delta = |g_F| \mu \Delta_B / \hbar$, where g_F is the Landé g factor, μ is the Bohr magneton, Δ_B is the shift in the magnetic field from resonant coupling condition, and $\hbar = \hbar / 2\pi$, gave us an experimentally controllable 5D parameter space labeled by the Cartesian coordinates $\mathbf{q} = (-\Omega_B \cos \phi_B, -\Omega_A \cos \phi_A, -\Omega_A \sin \phi_A, \delta, -\Omega_B \sin \phi_B)$. In much the same way that a two-level atom in a magnetic field can be understood in terms of three Pauli matrices, our four-level system is governed by the Hamiltonian

$$\hat{H} = -\frac{\hbar}{2} \mathbf{q} \cdot \hat{\Gamma} = -\frac{\hbar}{2} (q_1 \hat{\Gamma}_1 + q_2 \hat{\Gamma}_2 + q_3 \hat{\Gamma}_3 + q_4 \hat{\Gamma}_4 + q_5 \hat{\Gamma}_5) \tag{4}$$

where q_i and $\hat{\Gamma}_i$ ($i = 1, 2, \dots, 5$) are the i th components of \mathbf{q} and $\hat{\Gamma}$ is represented as the four-by-four Dirac matrices with the hyperfine ground states shown in Fig. 2A taken as the basis. Furthermore, because each of the Dirac matrices

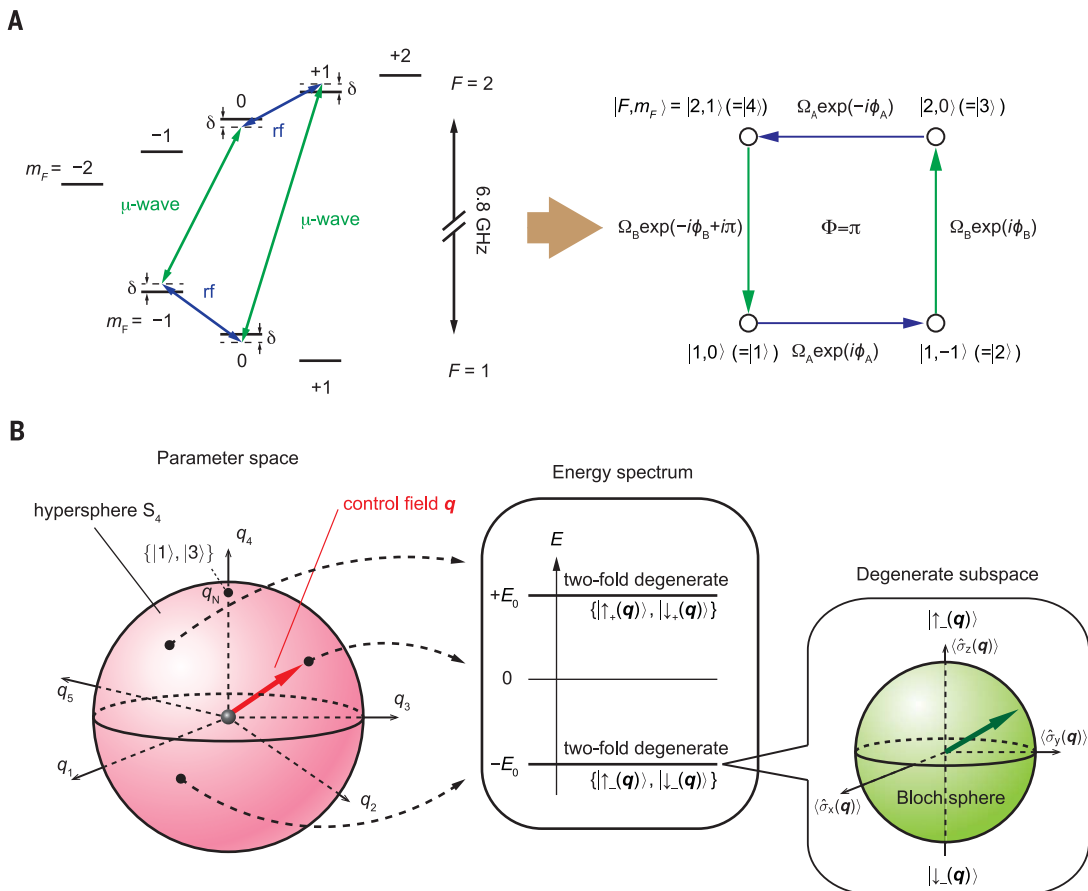
commutes with the time-reversal operator, the system has time-reversal symmetry (15); Kramers theorem then implies that the system has two pairs of degenerate energy states, here with energies $E_\pm = \pm \hbar |\mathbf{q}| / 2$. Thus, each energy, labeled by + or -, has two independent eigenstates $|\uparrow^\pm(\mathbf{q})\rangle$ and $|\downarrow^\pm(\mathbf{q})\rangle$; each of these pairs define a degenerate subspace (DS). As shown in Fig. 2B, these DSs are characterized by a generalized magnetization vector $\langle \Gamma \rangle = (\langle \hat{\Gamma}_1 \rangle, \langle \hat{\Gamma}_2 \rangle, \langle \hat{\Gamma}_3 \rangle, \langle \hat{\Gamma}_4 \rangle, \langle \hat{\Gamma}_5 \rangle)$ on a unit 4-sphere in our 5D space. Different configurations within each DS share the same magnetization vector, which can be pictured in terms of an additional 3D Bloch sphere (green sphere in Figs. 1 and 2B). An eigenstate is fully depicted by assigning the two such “Bloch” vectors. The Yang monopole (16, 17) resides at the Hamiltonian’s degeneracy point at $\mathbf{q} = 0$, a singular point where the non-Abelian Berry’s connection diverges. The non-Abelian Berry’s curvatures from our experimental Hamiltonian (Eq. 4) quantum simulates the fields of a Yang monopole.

Quantum control and measurement

We begin by demonstrating the control and measurement capabilities of our system. We first prepared the system in its ground state at the position $\mathbf{q}_0 = q_0(-1, -1, 0, 0, 0) / \sqrt{2}$ in parameter space, where the generalized magnetization is $\langle \Gamma \rangle = (-1, -1, 0, 0, 0) / \sqrt{2}$. Then, by ramping ϕ_A , we slowly moved the control vector around the

Fig. 2. Schematics of the experiment.

(A) Schematic of our implemented coupling using four hyperfine ground states of rubidium-87. The four states were cyclically coupled with radio-frequency (rf) and microwave fields. The right panel shows the resulting plaquette and the associated coupling parameters. (B) At any point in the 5D parameter space, the energy spectrum forms a pair of twofold degenerate manifolds with the energy gap equal to $\hbar|\mathbf{q}|$, where \mathbf{q} is the control field. Each degenerate subspace can be represented by a Bloch sphere.



circle $q(t) = q_0[-1, -\cos(2\pi t/T), -\sin(2\pi t/T), 0, 0]/\sqrt{2}$ shown in Fig. 3A, where T is the full ramp time, and $q_0 = |q_0| = 2\pi \times 2\text{kHz}$.

After preparing the eigenstate $(|\uparrow^-(\mathbf{q}_0)\rangle + i|\downarrow^-(\mathbf{q}_0)\rangle)/\sqrt{2} = (\sqrt{2}|1\rangle - (1+i)|2\rangle + i\sqrt{2}|3\rangle + (1-i)|4\rangle)/(2\sqrt{2})$ in the ground DS by rotating the control field (15) from the north pole $\mathbf{q}_N = q_0(0, 0, 1, 0)$, we measured the state for different evolution times in this nearly adiabatic ramp (Fig. 3B), and identified the orientation within the DS by performing quantum state tomography, giving the expectation values of the Pauli operators $\hat{\sigma}_i$ ($i = x, y, z$) in the ground DS at \mathbf{q}_N . As seen in

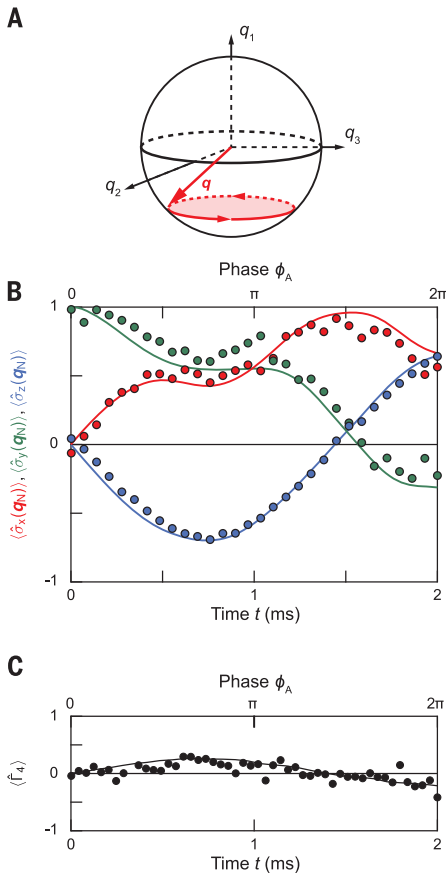


Fig. 3. State evolution under a non-Abelian gauge field. (A) Schematic of the control field trajectory. The two phases (ϕ_A, ϕ_B) were ramped for $T = 2$ ms with the laboratory parameters $\Omega_A/2\pi = \Omega_B/2\pi = 1.41$ kHz and $\delta = 0$. (B) Nearly-adiabatic response of pseudospin magnetization within the ground DS Bloch sphere, showing the nontrivial acquisition of a Wilczek-Zee phase after a 2π -rotation. The solid lines simulate the experiment by numerically solving the TDSE (15). (C) Deflection during the phase ramp. The state was slightly deflected along $\langle \hat{\Gamma}_4 \rangle$, resulting from our finite ramp time (black circles), changing from positive to negative. The black curve shows the theoretically expected linear response based on Eq. 6 (15).

Fig. 3B, after the control field completed one cycle, the orientation of the state vector within the DS differed from its initial value. After one cycle, the Berry's phase from an Abelian gauge field would contribute only an overall phase, leaving the state vector otherwise unchanged. In agreement with our numerical simulation obtained by solving (15) the time-dependent Schrödinger equation (TDSE) for the Hamiltonian in Eq. 4 (curves in Fig. 3B), this shows that the observed evolution resulted instead from the Wilczek-Zee phase derived from a non-Abelian gauge field.

We then measured $\langle \hat{\Gamma}_4 \rangle$ during this ramp and noted a small deflection of the magnetization of the state vector owing to remnant nonadiabatic effects (Fig. 3C). In linear response theory, deviations from adiabaticity can be described in terms of the response of the state vector to a general-

ized force $\hat{M}_\mu = -(\partial \hat{H} / \partial q_\mu) / \hbar$ acting on the state (Fig. 1B). For a conventional Abelian system, the local force at a fixed time (18, 19)

$$\langle \hat{M}_\mu \rangle = v_\nu F_{\mu\nu} + \text{constant} \quad (5)$$

resulting from parameters q_i , changing with velocity v_ν is analogous to the Lorentz force. This relation gives the driving force behind the topological and geometrical charge pumps recently realized in ultracold atoms (20–22). In both crystalline and optical lattices, the same relation underlies the anomalous quantum Hall effect (23–25).

Owing to the phase symmetry of the system for ϕ_A , the generalized geometric force from Eq. 5 is constant for our trajectory, inconsistent with the sign change present in the observed deflection (Fig. 3C). To account for this discrepancy, Eq. 5 can be extended to accommodate non-Abelian gauge fields, giving the generalized geometric force (15, 26)

$$\langle \hat{M}_\mu \rangle = v_\nu \langle \hat{F}_{\mu\nu} \rangle + \text{constant} \quad (6)$$

acting on the state, where the expectation value on the right-hand side is taken for a pure state at adiabaticity and $\hat{F}_{\mu\nu}$ is the Berry curvature of the associated degenerate subspace (26). In contrast to the Abelian case, where the generalized geometric force is simply the product of the local Berry curvature and the velocity, the force in Eq. 6 also depends on the quantum state within the DS. As we saw, even for adiabatic motion, Wilczek-Zee phases can lead to considerable evolution within the DS, making Eq. 6 essential for describing generalized geometric forces.

The sign change in Fig. 3C is now explained by the dependence of the geometric force on the state as it evolved within the DS. If the gauge field is Abelian, independent of the state within the DS, the force components should be constant in the spherical coordinate along the path for constant ramp velocity. The sign change reveals that the quantum state acquired a Wilczek-Zee phase from a non-Abelian gauge potential, contributing to the geometric force. Indeed, the solid curves depict the prediction of our TDSE simulations (15) and confirm that the geometric force in our experiment cannot be derived from an Abelian gauge potential.

In general, we can observe the full magnetization of the state vector by carefully measuring the expectation values (15) of all five operators $\hat{\Gamma}_i$. To demonstrate this capability, we moved along the circle $\mathbf{q}(t) = q_0[-\cos(2\pi t/T), -\cos(2\pi t/T), -\sin(2\pi t/T), 0, \sin(2\pi t/T)]/\sqrt{2}$ shown in Fig. 4A, starting from $|\uparrow^-(\mathbf{q}_0)\rangle = (|\sqrt{2}|1\rangle - |2\rangle + |4\rangle)/2$ at $t = 0$, and obtained $\langle \hat{\Gamma}(t) \rangle$. Figure 4B shows that $\langle \hat{\Gamma}(t) \rangle$ nearly followed the adiabatic trajectory (red curves), almost oriented parallel to \mathbf{q} , but slightly deflected owing to the nonadiabaticity [TDSE simulation (15) shown by black curves in Fig. 4B].

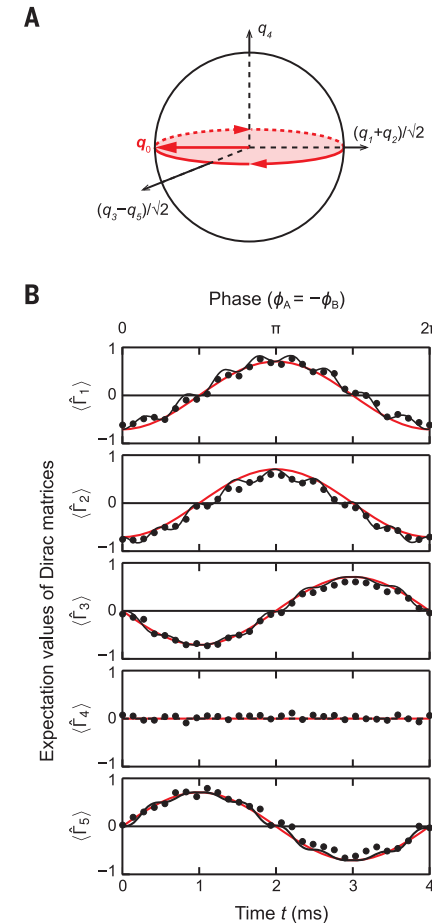


Fig. 4. Generalized magnetization. (A) Schematic of the control field trajectory. The two phases (ϕ_A, ϕ_B) are ramped for $T = 4$ ms with the laboratory parameters $\Omega_A/2\pi = \Omega_B/2\pi = 1.41$ kHz and $\delta = 0$. (B) Quantum states were measured by evaluating the expectation values of the five Dirac matrices. The red curves plot the trajectories expected for adiabatic motion, whereas the black curves are numerical simulations, including our finite ramp time (15).

Non-Abelian Berry curvatures and Chern numbers

With the ultimate goal of evaluating Chern numbers in mind, we characterized the non-Abelian Berry curvatures on spherical manifolds in parameter space. Accordingly, we adopt spherical coordinates described by a radius q and four angles $\theta_1 \in [0, \pi]$, $\theta_2 \in [0, \pi/2]$, ϕ_1 , and ϕ_2 that are related to our experimental control parameter space via $\Omega_A = q \sin \theta_1 \cos \theta_2$, $\Omega_B = q \sin \theta_1 \sin \theta_2$, $\delta = q \cos \theta_1$, $\phi_1 = (\phi_A + \phi_B)/2$, and $\phi_2 = (\phi_A - \phi_B)/2$.

After preparing the system in its ground state at \mathbf{q}_0 , we measured the deflection along the θ_1 direction, while rotating the control field along $\mathbf{q}_\pm(t) = q_0[-\cos(2\pi t/T), -\cos(2\pi t/T), \mp \sin(2\pi t/T), 0, \mp \sin(2\pi t/T)]/\sqrt{2}$ by ramping ϕ_1 from 0 to $\pm\pi$ (half-circles in Fig. 5A). The geometric force M_{θ_1} is directly obtained from the deflection of $\langle \hat{\Gamma}_4 \rangle$. Figure 5B plots the deflection during this ramp for four different initial states (marked by |A>, |B>, |C>, and |D) in Fig. 5D) within the DS, manifesting the state dependence of the geometric force in the non-Abelian gauge field in contrast to Abelian cases. The net deflection during any given ramp gives the integrated geometric force.

To confirm that our drive was in the linear response regime, we measured the geometric force as a function of ramp time T (Fig. 5C). From both the data and TDSE simulations (dashed curves), the geometric force (solid curves) is almost linear with respect to velocity for $T \geq 12\pi/q$.

The components of the Berry curvatures can be reconstructed from the integrated geometric force. Owing to the symmetry of our experimental Hamiltonian, the geometric force components must be almost constant in spherical coordinates during the ramp in the linear response regime. By measuring the geometric force experienced by four independent initial states all within the DS, we determined the four independent parameters present in the 2-by-2 matrices describing each element (labeled by β and γ) of the representation of the non-Abelian Berry curvature $F_{\mu\nu}^{\beta\gamma}$. Following this procedure for $T \geq 12\pi/q$, we obtained $2q_0^2 \hat{F}_{\theta_1\phi_1} = 0.01(3)\hat{I}_0 + [-0.06(5), 0.08(5), 0.98(3)] \cdot \hat{\sigma}$, in agreement with the theoretical value, $2q_0^2 \hat{F}_{\theta_1\phi_1} = \hat{\sigma}_z$ (here, \hat{I}_0 is the identity operator).

We thoroughly investigated the state dependence of the geometric force by studying the evolution of 225 initial states covering the Bloch sphere of the initial DS (Fig. 5D). For each initial state, we recorded the deflection after a 250- μ s ramp to obtain the Berry curvature component $\langle \hat{F}_{\theta_1\phi_1} \rangle$. Figure 5D shows the initial-state Bloch sphere colored according to the curvature; the theoretically computed result (top) is in good agreement with experimental result (bottom).

By changing the path and the direction along which we measure the deflection, other components of the curvatures can be measured. For example, by rotating the control field along $\mathbf{q}_\pm(t) = q_0[-\cos(2\pi t/T), -\cos(2\pi t/T), \mp \sin(2\pi t/T), 0, \pm \sin(2\pi t/T)]/\sqrt{2}$ by ramping ϕ_2 and evaluating the deflection along the θ_2 direction at \mathbf{q}_0 , we obtained $2q_0^2 \hat{F}_{\theta_2\phi_2} = -0.08(3)\hat{I}_0 + [-0.12(5),$

$-0.07(5), 1.00(3)] \cdot \hat{\sigma}$, also in good agreement with the theoretical value, $2q_0^2 \hat{F}_{\theta_2\phi_2} = \hat{\sigma}_z$.

Just as in classical electromagnetism, where the fields from electric or magnetic sources fall off as $1/q^2$, the non-Abelian gauge field strength also follows a $1/q^2$ scaling law, as required by the generalized Gauss's law (see Eq. 2) that defines the second Chern number. By repeating the same Berry curvature measurement ($\hat{F}_{\theta_2\phi_2}$) for different q_0 , while keeping $2\pi/qT = 0.25$ constant to remain in the linear response regime, the Berry curvature components ($\hat{F}_{\theta_2\phi_2}$) indeed had the $1/q^2$ scaling of a monopole source (Fig. 5E); this also suggests that $\langle \hat{F}_{\theta_2\phi_2} \rangle$ diverges at $q \rightarrow 0$.

Taken together, these fields provide sufficient information to extract the second Chern number of a 4-sphere with radius q_0 . We evaluate the second Chern number using the relation

$$C_2 = \frac{3q_0^4}{4\pi^2} \int_{S_4} \text{tr}[F_{\theta_1\theta_1} F_{\theta_2\theta_2}] d^4S \quad (7)$$

where S_4 defines the 4-sphere and $d^4S = \sin^3 \theta_1 \sin 2\theta_2 d\theta_1 d\theta_2 d\phi_1 d\phi_2$. Equation 7 relies on the rotational symmetry of $\hat{H}(\mathbf{q})$, which gives the numerically confirmed (15) relations $\text{tr}[F_{\theta_1\theta_1} F_{\theta_2\theta_2}] = \text{tr}[F_{\theta_1\theta_2} F_{\theta_2\theta_1}] = \text{tr}[F_{\theta_1\theta_2} F_{\theta_2\theta_1}]$. From the non-Abelian Berry curvature measurements in the

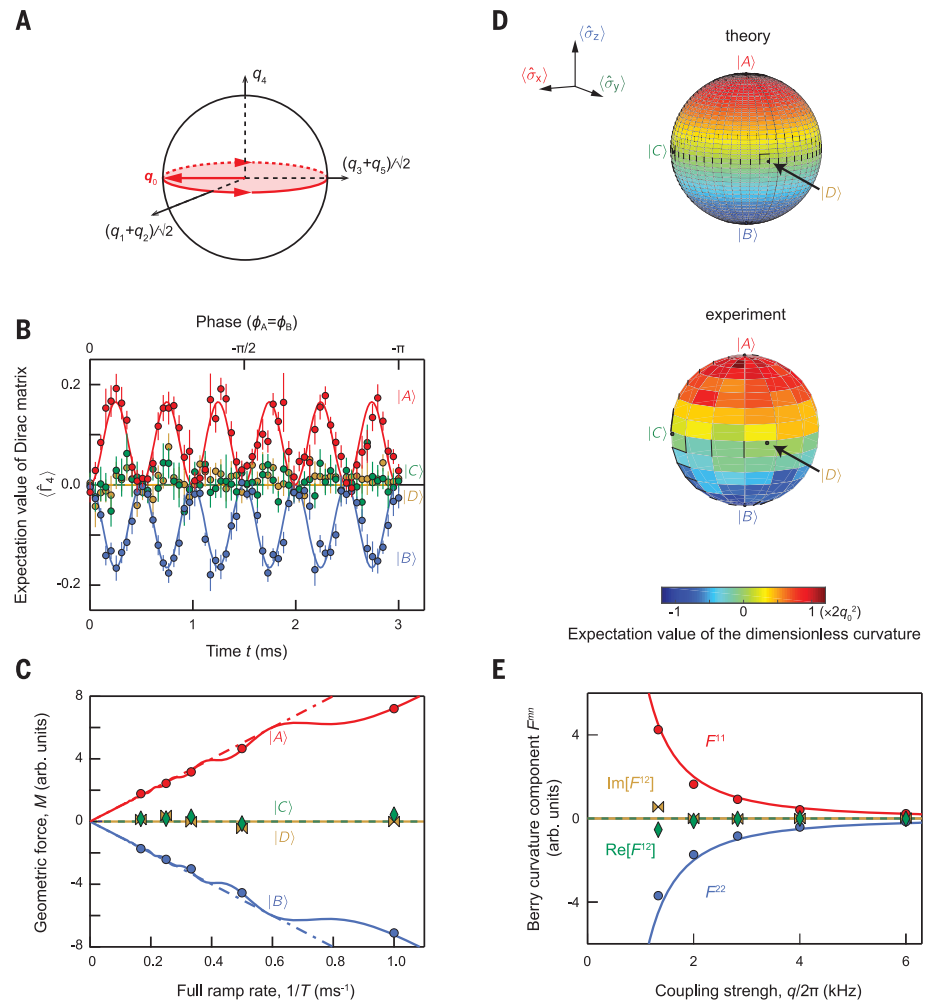


Fig. 5. Deflection of states within the ground-state manifold owing to non-Abelian Berry curvatures. (A) Schematic of the control field trajectory. (B) Deflections along θ_1 were measured during the $T = 6$ ms ramp. $\langle \hat{\Gamma}_4 \rangle$ was measured for four independent initial states (|A>, |B>, |C>, and |D>) within the DS at \mathbf{q}_0 . Here |A> = $(\sqrt{2}(|1\rangle - |2\rangle + |4\rangle))/2$ and |B> = $(-|2\rangle + \sqrt{2}(|3\rangle - |4\rangle))/2$ are the basis states for the DS, |C> = $(|A\rangle + |B\rangle)/\sqrt{2}$, and |D> = $(|A\rangle + i|B\rangle)/\sqrt{2}$. (C) Geometric force as a function of $1/T$ measured for the four initial states (|A>, |B>, |C>, and |D>) at \mathbf{q}_0 . The dashed lines assume linearity, and the solid curves are the outcomes of our TDSE simulations (15). (D) Expectation values of the non-Abelian Berry curvature ($\hat{F}_{\theta_1\phi_1}$) in the ground state manifold at \mathbf{q}_0 are mapped onto Bloch spheres associated with the state within the DS at \mathbf{q}_0 . The four initial states used in (A) to (C) are also shown in the theoretical (top sphere) and the experimental (bottom sphere) plots. (E) $1/q^2$ scaling in the strength of the curvature. The matrix components of the curvature ($\hat{F}_{\theta_2\phi_2}$) are evaluated for various q_0 . The data show excellent agreement with the theory that exhibits $1/q^2$ dependence (solid lines).

previous section, we directly obtained $C_2 = 2q_0^2 \text{tr}[F_{\theta_1\phi_1}(\mathbf{q}_0)F_{\theta_2\theta_2}(\mathbf{q}_0)] = 0.97(6)$ for the ground state, consistent with the theoretical value $C_2 = 1$. We repeated the measurements for the excited state and found $C_2 = 2q_0^2 \text{tr}[F_{\theta_1\theta_2}(\mathbf{q}_0)F_{\phi_2\phi_1}(\mathbf{q}_0)] = -0.93(6)$, also in agreement with the theoretical value $C_2 = -1$. These nonzero Chern numbers inform us that the manifold is topologically nontrivial.

Because the system is time-reversal symmetric, the first Chern form is zero, and therefore Eq. 3 for the first Chern number should be zero for both degenerate manifolds. Indeed, all the measured non-Abelian Berry curvatures were traceless ($q_0^2 \text{tr}[\hat{F}_{\theta_2\theta_2}] = -0.08(3)$ and $q_0^2 \text{tr}[\hat{F}_{\theta_1\phi_1}] = 0.01(3)$ for the ground state, and $q_0^2 \text{tr}[\hat{F}_{\theta_1\theta_2}] = -0.02(3)$ and $q_0^2 \text{tr}[\hat{F}_{\phi_2\phi_1}] = 0.00(3)$ for the excited state), so that the first Chern number, which is the surface integral of the trace of the

individual curvatures, was also zero. Thus, the nontrivial topology of the monopole field is not expressed by a first Chern number.

Topological transition

We concluded our measurements by inducing a topologically nontrivial-to-trivial transition of the manifold by displacing the 4-sphere in parameter space from the origin by an amount $\mathbf{q}_{\text{offset}} = q_{\text{offset}}(\mathbf{q}_0/q_0)$ (Fig. 6A). The topological transition occurs at the critical displacement $q_{\text{crit}} = q_0$ when the Yang monopole departs the manifold. Figure 6B shows our observed transition of the second Chern number from ± 1 , for the ground and excited states, to zero as the offset coupling q_{offset} was increased. This transition is associated with the topology of the manifold changing from topologically nontrivial to trivial. The smoothness of the observed transition was

caused by the breakdown of the linear response near the transition point. Our theory [continuous curves in Fig. 6B, and see (15)] shows that slower ramps enlarge the region in which linear response is valid and make the transition sharper (Fig. 6B). Topological transitions have been observed in a range of experiments (6, 7, 25); however, in all of these cases, the observed topological phases were only identified by a Dirac monopoles' first Chern number and enclosing 2D manifolds. By contrast, in our system, the first Chern number is zero everywhere and the second Chern number characterizes the topological phase, arising from a Yang monopole at the origin of parameter space. The opposite topological charges observed in the ground or excited manifolds result from a monopole in one manifold acting as an antimonopole in the other. With these Chern number measurements, we confirmed that the engineered topological singularity in our system indeed simulated a Yang monopole.

Discussion and outlook

Our work can be extended to other quantum systems, including ions, thermal atoms, and superconducting qubits. The Chern number characterizes a source of gauge field with high symmetry, a symmetry that naturally arises in particle physics in contexts such as quantum chromodynamics.

The monopole field and the second Chern number have been discussed theoretically in the context of 4D quantum Hall effect (4DQH) (27, 28), spin-Hall effect (29), exotic charge pumping (30), and fermionic pairing (31) in condensed matter systems. The model we explored experimentally is equivalent to the (4 + 1)-D lattice Dirac Hamiltonian relevant to 4DQH. The 4DQH is a generalized quantum Hall effect and is the root state of a family of topological insulators, which are obtained by a dimensional reduction procedure (32). The observed transition in Fig. 6B can be regarded as the type of phase transition present in the band topology of 4DQH systems. A conformal mapping from a 4D spherical manifold in parameter space to a 4D crystal momentum space, 4-torus, directly recasts our Hamiltonian as the Dirac Hamiltonian.

Our observation lays the groundwork for simulating objects in high-energy physics with atomic quantum systems. Lattice extensions of our work, where lattice sites or bands play the role of spin states, may allow quantum simulation of emergent many-body dynamics with non-Abelian gauge fields with highly controllable ultracold quantum gases systems (33–36).

REFERENCES AND NOTES

1. C. N. Yang, R. L. Mills, *Phys. Rev.* **96**, 191–195 (1954).
2. G. 't Hooft, *Nature* **448**, 271–273 (2007).
3. G. 't Hooft, *Nucl. Phys. B* **79**, 276–284 (1974).
4. P. A. M. Dirac, *Proc. R. Soc. Lond. Ser. A* **133**, 60–72 (1931).
5. M. W. Ray, E. Ruokokoski, S. Kandel, M. Möttönen, D. S. Hall, *Nature* **505**, 657–660 (2014).
6. M. D. Schroer et al., *Phys. Rev. Lett.* **113**, 050402 (2014).
7. P. Roushan et al., *Nature* **515**, 241–244 (2014).
8. Y. Aharonov, D. Bohm, *Phys. Rev.* **115**, 485–491 (1959).
9. C. N. Yang, *J. Math. Phys.* **19**, 320–328 (1978).
10. N. Manton, P. Sutcliffe, *Topological Solitons* (Cambridge Univ. Press, 2004).

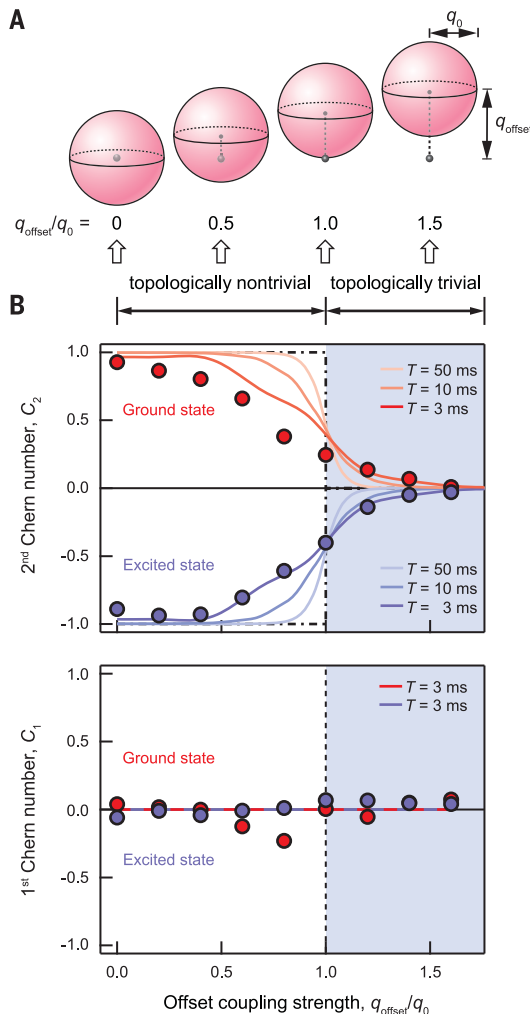


Fig. 6. Topological transition from a Yang monopole. (A) Schematic illustration of the topological transition. Suitable spherical manifolds with radius q_0 were offset from the origin by q_{offset} to evaluate both C_1 and C_2 . At the critical value ($q_{\text{crit}} = q_0$), the monopole exits the manifolds. (B) Chern numbers extracted from experiment. When the manifold crossed $q_{\text{crit}} = q_0$, $|C_2|$ decreased from unity to zero (top panel), whereas C_1 was constantly zero for both the ground (red) and the excited (blue) states (bottom panel). Numerical simulations (solid lines; $T = 3, 10,$ and 50 ms) and analytic theory (dash-dot lines) are also shown. The data were taken for $T = 3$ ms.

11. M. V. Berry, *Proc. R. Soc. Lond. Ser. A* **392**, 45–57 (1984).
12. F. Wilczek, A. Zee, *Phys. Rev. Lett.* **52**, 2111–2114 (1984).
13. K. Toyoda, K. Uchida, A. Noguchi, S. Haze, S. Urabe, *Phys. Rev. A* **87**, 052307 (2013).
14. T. Li *et al.*, *Science* **352**, 1094–1097 (2016).
15. See supplementary materials.
16. Y. Hatsugai, *New J. Phys.* **12**, 065004 (2010).
17. Our non-Abelian gauge field is SU(2) symmetric, where the generator can be, for example, the Pauli matrices.
18. V. Gritsev, A. Polkovnikov, *Proc. Natl. Acad. Sci. U.S.A.* **109**, 6457–6462 (2012).
19. J. E. Avron, M. Fraas, G. M. Graf, O. Kenneth, *New J. Phys.* **13**, 053042 (2011).
20. H.-I. Lu *et al.*, *Phys. Rev. Lett.* **116**, 200402 (2016).
21. M. Lohse, C. Schweizer, O. Zilberberg, M. Aidelsburger, I. Bloch, *Nat. Phys.* **12**, 350–354 (2016).
22. S. Nakajima *et al.*, *Nat. Phys.* **12**, 296–300 (2016).
23. N. Nagaosa, J. Sinova, S. Onoda, A. H. MacDonald, N. P. Ong, *Rev. Mod. Phys.* **82**, 1539–1592 (2010).
24. G. Jotzu *et al.*, *Nature* **515**, 237–240 (2014).
25. M. Aidelsburger *et al.*, *Nat. Phys.* **11**, 162–166 (2015).
26. M. Kolodrubetz, *Phys. Rev. Lett.* **117**, 015301 (2016).
27. S.-C. Zhang, J. Hu, *Science* **294**, 823–828 (2001).
28. H. M. Price, O. Zilberberg, T. Ozawa, I. Carusotto, N. Goldman, *Phys. Rev. B* **93**, 245113 (2016).
29. S. Murakami, N. Nagaosa, S.-C. Zhang, *Phys. Rev. B* **69**, 235206 (2004).
30. Y. E. Kraus, Z. Ringel, O. Zilberberg, *Phys. Rev. Lett.* **111**, 226401 (2013).
31. C.-H. Chern, H.-D. Chen, C. Wu, J.-P. Hu, S.-C. Zhang, *Phys. Rev. B* **69**, 214512 (2004).
32. X.-L. Qi, T. L. Hughes, S.-C. Zhang, *Phys. Rev. B* **78**, 195424 (2008).
33. Y.-J. Lin *et al.*, *Phys. Rev. Lett.* **102**, 130401 (2009).
34. J. Ruseckas, G. Juzeliūnas, P. Öhberg, M. Fleischhauer, *Phys. Rev. Lett.* **95**, 010404 (2005).
35. P. Hauke *et al.*, *Phys. Rev. Lett.* **109**, 145301 (2012).
36. E. A. Martinez *et al.*, *Nature* **534**, 516–519 (2016).

ACKNOWLEDGMENTS

The authors would like to thank A. Polkovnikov and M. Kolodrubetz for discussion. **Funding:** This work was partially supported by the U.S. Army Research Office's Atomtronics MURI, and by the U.S. Air Force Office of Scientific Research's Quantum Matter MURI, National Institute of Standards and Technology, and NSF through the Physics Frontier Center at the Joint Quantum

Institute. S.S. acknowledges the Japan Society for the Promotion of Science (fellowship for research abroad). **Author contributions:** S.S. conducted the experiment, performed the theoretical work, and analyzed the data. S.S., A.R.P., F.S.-C., and I.B.S. contributed to the rubidium Bose-Einstein condensate apparatus. All authors substantially participated in the discussion and the writing of the manuscript. S.S. and I.B.S. conceived of the project. **Competing interests:** The authors declare no competing interests. **Data and materials availability:** All data are available in the manuscript or the supplementary materials.

SUPPLEMENTARY MATERIALS

www.sciencemag.org/content/360/6396/1429/suppl/DC1
Materials and Methods
Supplementary Text
Figs. S1 to S3
References (37, 38)
Database S1

15 February 2017; accepted 27 April 2018
10.1126/science.aam9031

Second Chern number of a quantum-simulated non-Abelian Yang monopole

Seiji Sugawa, Francisco Salces-Carcoba, Abigail R. Perry, Yuchen Yue and I. B. Spielman

Science **360** (6396), 1429-1434.

DOI: 10.1126/science.aam9031

Going beyond the first Chern number

Topological properties of physical systems are reflected in so-called Chern numbers: A nonzero Chern number typically means that a system is topologically nontrivial. Sugawa *et al.* engineered a cold atom system with a nonzero second Chern number, in contrast to condensed matter physics, where only the first Chern number is usually invoked. The exotic topology relates to the emergence of a type of magnetic monopole called the Yang monopole (known from theoretical high-energy physics) in a five-dimensional space of internal degrees of freedom in a rubidium Bose-Einstein condensate. The results illustrate the potential of cold atoms physics to simulate high-energy phenomena.

Science, this issue p. 1429

ARTICLE TOOLS

<http://science.sciencemag.org/content/360/6396/1429>

SUPPLEMENTARY MATERIALS

<http://science.sciencemag.org/content/suppl/2018/06/27/360.6396.1429.DC1>

REFERENCES

This article cites 35 articles, 5 of which you can access for free
<http://science.sciencemag.org/content/360/6396/1429#BIBL>

PERMISSIONS

<http://www.sciencemag.org/help/reprints-and-permissions>

Use of this article is subject to the [Terms of Service](#)